bonding effects, (ii) the polarization of electrons around both the Mn$2p_{3/2}$ and O$1s$ holes involved, and (iii) a more realistic treatment of the many-electron wave functions involved in the dipole and coulomb matrix elements, including configuration interaction effects. Theory also predicts a variation of the resonance effects with photoelectron emission angle due to photoelectron diffraction effects that is at least qualitatively seen in our data for the azimuthal angle (ϕ) dependence of intensities on and off the Mn$2p_{3/2}$ resonance (*21*). Finally, our theoretical analysis suggests that these effects will die off approximately as 1/(distance-to-neighbor)^3. Thus, MARPE should be primarily sensitive to the nearest neighbors of a certain type of atom, and the observation of it should permit directly determining the atomic number of these nearest neighbors. Some next-nearest-neighbor sensitivity is also evident, as seen in our data for $La_{0.7}Sr_{0.3}MnO_3$ between Mn and La (see Fig. 3E).

Several future directions of exploration and application of this effect can be pointed out. MARPE intensity enhancements are expected to be very sensitive to small changes in bond distances, bonding type, or both; for example, it may be possible to study the changes in the Mn-O distance thought to occur in the colossal magnetoresistive materials due to Jahn-Teller distortions (*22*). The well-known chemical shifts in photoelectron kinetic energies (*3*) should also permit measurement of resonances separately around different chemically distinct species. Although we used single crystals to better define the present data, there is no general requirement of a single-crystal specimen, thus broadening applicability considerably. MARPE effects should also be observable in free molecules, probably with reduced intensity if the number of near neighbors of a given type is lower, but perhaps with enhanced intensity if the resonant excited level is a more delocalized molecular orbital which better couples the several atoms involved. Here, we used photoelectrons emitted from the near-surface region to detect these resonances, but they should also be present in secondary fluorescent soft x-rays or Auger electrons resulting from the filling of the primary hole on the emitter. With x-ray detection, the experiment would become more bulk sensitive, considerably widening its applicability to include perhaps systems of biological interest, although a careful allowance for the enhanced absorption of the exciting flux at resonance would be needed to unambiguously detect the resonant enhancement. Atoms at buried interfaces should also be directly detectable via MARPE between a constituent of one side of the interface and a constituent of the other side. Finally, exciting with circularly polarized radiation on magnetic samples should lead to resonant photoelectron spin polarization or magnetic dichroism effects, or both, in these resonances, yielding a probe of near-neighbor magnetic order.

References and Notes

1. E. A. Stern, M. Newville, B. Ravel, Y. Yacoby, D. Haskel, *Physica B* **208-209**, 117 (1995); M. Newville *et al.*, *ibid.*, p. 154; and references therein.
2. M. A. Van Hove, W. H. Weinberg, C.-M. Chan, *Low Energy Electron Diffraction* (Springer-Verlag, Heidelberg, Germany, 1986).
3. C. S. Fadley *et al.*, *Prog. Surf. Sci.* **54**, 341 (1997), and references therein.
4. U. Fano and J. W. Cooper, *Rev. Mod. Phys.* **40**, 493 (1968).
5. M. O. Krause, T. A. Carlson, A. Fahlman, *Phys. Rev. A* **30**, 1316 (1984), and references therein.
6. L. J. Garvin, E. R. Brown, S. L. Carter, H. P. Kelly, *J. Phys. B* **16**, L269 (1983).
7. A. Tanaka and T. Jo, *J. Phys. Soc. Jpn.* **63**, 2788 (1994), and references therein.
8. M. Weinelt *et al.*, *Phys. Rev. Lett.* **78**, 967 (1997), and references therein.
9. S. M. Butorin, J.-H. Guo, M. Magnuson, P. Kuiper, J. Nordgren, *Phys. Rev. B* **54**, 4405 (1996).
10. Z. Hussain *et al.*, *J. Electron Spectrosc. Relat. Phenom.* **80**, 401 (1996).
11. C. J. Powell, A. Jablonski, S. Tanuma, D. R. Penn, *ibid.* **68**, 605 (1994).
12. C. J. Powell, personal communication.
13. J. Stohr and R. Nakajima, *IBM J. Res. Dev.* **42**, 73 (1998).
14. J. Kortright, unpublihed results for Fe.
15. E. Gullikson, Center for X-ray Optics, Lawrence Berkeley National Laboratory, public access program for calculating x-ray penetration depths and reflectivities available at www-cxro.lbl.gov
16. P. Kuiper, B. G. Searle, P. Rudolf, L. H. Tjeng, C. T. Chen, *Phys. Rev. Lett.* **70**, 1549 (1993).
17. M. A. Brewer *et al.*, *Advanced Light Source Compendium of User Abstracts and Technical Reports*, Report LBNL-39981, UC-411 (Lawrence Berkeley National Laboratory, Berkeley, CA, 1997), p. 411; K. Krishnan, personal communication.
18. B. T. Thole *et al.*, *Phys. Rev. B* **32**, 5107 (1985).
19. A fuller treatment of MARPE theory is available as supplementary material via the *Science* Web site at www.sciencemag.org/feature/data/981789.shl
20. F. J. García de Abajo, in preparation.
21. A. Kay, E. Arenholz, S. Mun, C. S. Fadley, data not shown.
22. S. J. L. Billinge, R. G. DiFrancesco, G. H. Kwei, J. J. Neumeier, J. D. Thompson, *Phys. Rev. Lett.* **77**, 715 (1996).
23. We are indebted to M. P. Klein and J. Kortright for helpful discussions, and to S. A. Chambers and K. Krishnan for providing samples. Supported by the Office of Energy Research, Materials Sciences Division, of the U.S. Department of Energy, under contract DE-AC03-76SF00098. Additional support from the Miller Institute (E.A.), the D.F.G.-Germany (R.D.), and the Basque Government (F.J.G.deA.) is also gratefully acknowledged.

6 April 1998; accepted 9 June 1998

Visualization of Three-Dimensional Chaos

G. O. Fountain, D. V. Khakhar,* J. M. Ottino†

Most chaotic mixing experiments have been restricted to two-dimensional, time-periodic flows, and this has shaped advances in theory as well. A prototypical, bounded, three-dimensional flow with a moderate Reynolds number is presented; this system lends itself to detailed experimental observation and allows for high-precision computational inspection. The flow structure, captured by means of cuts with a laser sheet (experimental Poincaré section), was visualized with the use of continuously injected fluorescent dye streams and revealed detailed chaotic structures with high-period islands.

Mixing is important in industry and ubiquitous in nature. Mixing-related problems may account for from 0.5 to 3% of the $750 billion per year output value of U.S. chemical industries (*1*). In nature, examples of mixing include mantle convection (*2, 3*) and dispersion in oceans (*4, 5*) and in the atmosphere (*6, 7*). Over the last 10 years, there have been significant advances in our understanding of mixing (*8, 9*), which can be traced back to a clear connection between mixing and chaos as well as to careful experiments in prototypical flows (*10*). However, with few exceptions (*11, 12*), experiments have been restricted to two-dimensional (2D) time-periodic flows, and consequently this has shaped theoretical advances as well.

Studies with idealized 2D flows have helped visualize chaos and have been instrumental for many applications. In two dimensions passive dye structures in time-periodic flows evolve in an iterative fashion: an entire structure is mapped into a new structure that has persistent large-scale features but also finer and finer scale features that are revealed at each period of the flow. Unmixed regions (regular islands) translate, stretch, and contract periodically; they represent the primary obstacle to efficient mixing. Particle trajectories in chaotic regions separate exponentially fast, and material filaments are continuously stretched and folded by means of horseshoes (*10*). Formally, the advection equations are a

---

Laboratory for Fluid Mechanics, Chaos, and Mixing, Department of Chemical Engineering, McCormick School of Engineering and Science, Northwestern University, Evanston, IL 60208–3120, USA.

*Permanent address: Department of Chemical Engineering, Indian Institute of Technology–Bombay, Powai, Bombay 400076, India.

†To whom correspondence should be addressed. E-mail: ottino@chem-eng.nwu.edu

Hamiltonian system (*13*), for which considerable theory already exists (*14*); however, the 3D picture, is considerably less clear.

Even though the first theoretical example of chaotic advection was a 3D flow (*15*), the number of theoretical studies addressing chaos and mixing in such flows is small (*16–18*). One problem is that an experimentally tractable 3D system that allows for detailed experimental and computational investigation had not been available.

The system presented here is inspired by the studies of Bajer and Moffat (*19*) and Stone *et al.* (*20*) in which a flow within a spherical drop of a viscous fluid is induced by a combination of a 3D hyperbolic flow (*21*) and a twisting flow ω mimicking a vortical flow. The angle between the principal axis of compression or extension and the axis of rotation ω is denoted α. If $\alpha = 0$, the flow is regular, but if $\alpha > 0$, then the flow is chaotic (*19, 20*), with Poincaré sections (mappings formed by the repeated intersections of fluid trajectories with a specified surface) that show a classical picture of Kolmogorov-Arnold-Moser (KAM) tori and chaotic tangles (*22*).

The possibility of realizing the drop flow in laboratory experiments seems remote. The flow needs to be slow (Stokes regime), and this limits either the drop size (small) or the speed of the flow (slow). A simple system, the "fundamental mixing tank," contains the essential ingredients of the drop model and can be regarded as an idealized model of the radial-flow stirred tanks found in industrial practice (23). The apparatus consists of a cylindrical tank of diameter T with a flat disk impeller with diameter D. Both the impeller and the tank can be rotated at angular speeds Ω_I and Ω_T, respectively, and the angle of the impeller with respect to the vertical, α, can be changed. Two Reynolds numbers can be thus defined with respect to the impeller (I) and tank (T) angular speeds: $Re_I = \Omega_I D^2 \rho/\mu$, $Re_T = \Omega_T T^2 \rho/\mu$, where ρ and μ are the density and viscosity of the fluid, respectively (*24*). Both can be varied experimentally in the range $0 < Re_I < 150$, and $0 < Re_T < 10$. For the experiments reported here, $Re_T = 0$. The impeller's rotation creates a secondary flow, the von Kármán flow (downward above the disk and upward below it) (*25*) that impinges into the impeller and then moves radially outward while at the same time undergoing a twist. This results, in the case $\alpha = 0$, in circulation regions (nested-flow tori) above and below the impeller. If $\alpha > 0$, the system loses rotational symmetry but the circulation regions still persist. The experimental (PIV) and computed vector velocity fields agree well (Fig. 1). The interaction between the von Kármán flow and the toroidal flow results in chaos (Fig. 2). Experimental examples are shown in Figs. 3 and 4.

In our system the tank is 30 cm tall with a 13-cm inside diameter fabricated with 1/4-inch (0.635-cm) cast acrylic tube. The tank is supported only at the rim to allow for 360° viewing access (*26, 27*). The cross section of the flow is illuminated by a sheet of laser light (*28*). In addition, a mirror is used to reflect a portion of the sheet from below the system upward to illuminate the otherwise shadowed area behind the impeller shaft.

The primary fluid we used in our experiments was USP-grade glycerine. For the experimental PIV measurements (*29*), NaI was added at 17.7 weight % to alter the index of refraction of the glycerine to closely match that of the acrylic walls for the wavelength of the yttrium-aluminum-garnet (YAG) laser. Unless this step is taken, the optical distortions due to the curved tank wall reduce the accuracy of the velocity field measurements (Fig. 1).

We used laser-grade fluorescent dyes diluted in glycerine to visualize the flows. Because of the extremely low concentrations, density and viscosity variations are negligible. We selected the dyes fluorescein, fluorexon, rhodamine 6G, and sulforhodamine B for their absorption characteristics as well as for the color of their emissions. Another consideration was to minimize coupling be-

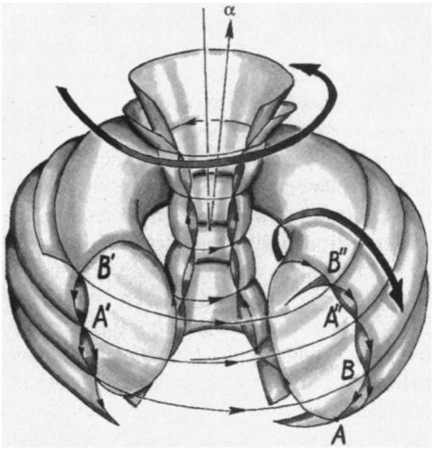

Fig. 2. Representation of connections between the toroidal circulation flow and the von Kármán flow, impinging upward on the rotating disk. The flow in the tank has two fixed points in the region below the impeller, both hyperbolic. When the flow is symmetric ($\alpha = 0$) the unstable manifold of the lower fixed point joins smoothly with the stable manifold of the upper point, and both coincide with the axis of symmetry. In this case the remaining trajectories lie on nested invariant tori. Perturbation of the geometry ($\alpha > 0$) results in chaos from two sources: the manifolds of the fixed points intersect, resulting in heteroclinic tangles near the axis, and some of the 1-tori break into higher order tori surrounded by homoclinic tangles. In the Poincaré section the 1-tori appear as closed curves and the higher order tori as a chain of islands (point A gets mapped to A′, A″, and so forth; similarly for point B). The tori with the most irrational winding numbers survive the greatest magnitude of perturbations.

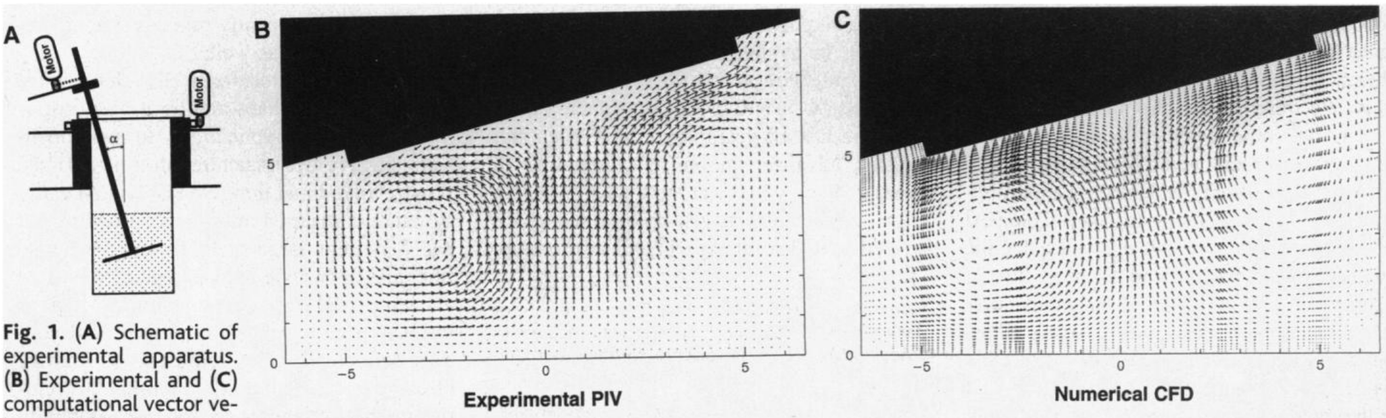

Fig. 1. (**A**) Schematic of experimental apparatus. (**B**) Experimental and (**C**) computational vector velocity fields for the region below the impeller. Conditions were $\alpha = 15°$, $\Omega_I = 29.5$ rpm, and $\Omega_T = 0$ rpm. The experimental velocity field was obtained from particle image velocimetry (PIV) by using a dual YAG laser system and digital image capture. Numerical results were obtained by finite element simulations with FIDAP on a fine grid of 300,000 nodes.

tween dyes where the emission of one (in-plane) dye can cause another (out-of-plane) dye to absorb and reemit, thus obscuring the view. In a run, different dyes were slowly injected into the flow with long 0.9- and 1.3-mm outer diameter thin wall needles (*30*). For each run, two to four injection needles were prepared and placed along the outer wall. Runs were conducted in one of two ways. In the first method all of the needles were positioned at the start of the experiment and all injections were made simultaneously. This approach minimizes any disturbances to the flow during the experiment and maintains an equal injection and diffusion time for all traces; however, the needles penetrating to the inner portions of the tori must cross the outer dye trace boundaries, which causes a slight folding effect. In the second method the needles were positioned sequentially starting near the center of the recirculation region and working outward one color at a time. This method minimizes the disturbances from the needle and allows for earlier traces to guide the placement of later ones; however, the traces no longer have the same advection times.

An example of the cross-sectional dye structure, along with numerically computed Poincaré sections, is shown in Fig. 3. Good agreement is seen between the experimental and the computed results; period-4 islands are clearly seen. The statistical limit—as ascertained, for example, by scaling of self-similar stretching distributions (*8*) (Fig. 5)—was obtained in about five axial circulation times even though the experimental results still revealed large-scale inhomogeneities. The results displayed in Figs. 3 and 4 show that circulation regions, as seen in streamline portraits (Fig. 1), do not even begin to capture the intricacy of advected dye structures.

Experimental visualization of the details of mixing in 3D flows has been difficult, because blobs of tracer introduced in the flow are quickly deformed into thin folded sheets, which quickly become invisible. (This is in contrast to 2D flows in which blobs remain unstretched perpendicular to the plane of the flow and hence remain visible even after being greatly stretched.) But in our experiments a small stream of tracer generates a streakline, which coincides with the trajectory (pathline) at the injection point. When a surface is illuminated, the intersections are revealed, and the result is, by definition, a Poincaré section (Fig. 3).

Several elements of the chaotic picture are easier to capture in 3D experiments than in 2D ones. KAM tori (islands of regularity in 2D cuts) are revealed clearly in 3D experiments and they are relatively straightforward to capture. High-period islands, easily observable in pictures such as Fig. 4C, are not easily captured in 2D experiments. It normally takes thousands of periods to define the contour of an island in numerically obtained Poincaré sections; moreover, the initial points should be carefully placed. On the other

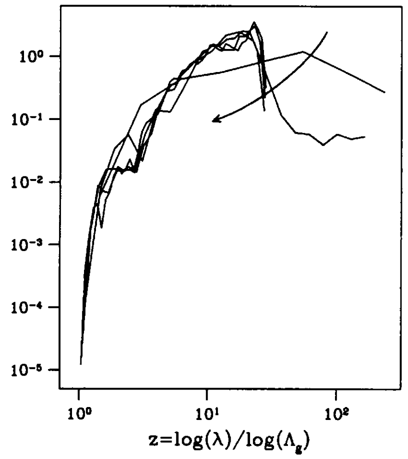

Fig. 5. Distribution of stretches within the flow at different times. The initial distribution is a delta function with the stretching set at a value of 1. The distribution is calculated by advecting 2500 randomly placed material elements in the region below the impeller and computing the deformation tensor for each. Stretching is computed for each trajectory along with the overall probability distribution for increasing amounts of advection time (indicated by the arrow). $\mathcal{H}_n$ is the scaled probability and Λ_g is the geometric mean stretch, which increases exponentially in time. Scaling reveals that the stretching is self-similar (*8*).

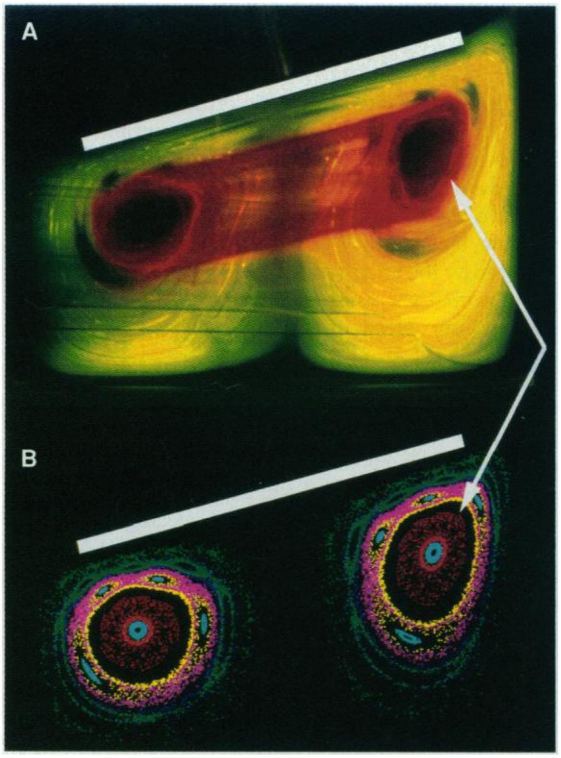

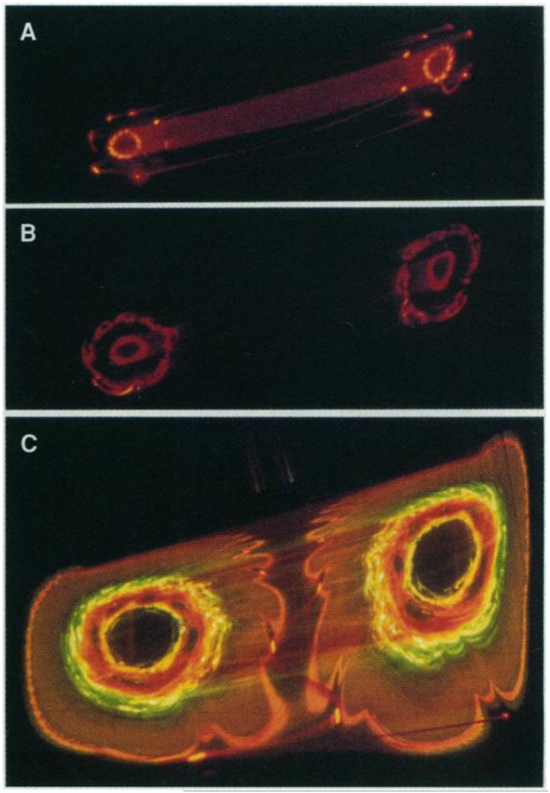

Fig. 3 (left). Experimental (**A**) and computational (**B**) Poincaré sections. The conditions are α = 14.3°, Ω_I = 33 rpm, and Re_I = 7.2. The experiment in (A) represents the result of two dye injections, one red and one green; the red dye was injected first and allowed to run before the green dye was injected. The arrow in (B) shows the location of a torus, seen edgewise in (A) as well. The buildup of the same torus, but obtained from different injection points than those here, is shown in Fig. 4, A and B. A different run, corresponding to a slightly different operating condition displaying period 6 islands, is shown in Fig. 4C. **Fig. 4 (right).** (**A** and **B**) Time evolution of the formation of the red torus in Fig. 3A obtained by different injection conditions; the torus is visualized here by means of two red dye injections. (**C**) Slightly different conditions than used in Fig. 3 (α = 14.3°, Ω_I = 18.6 rpm, Re_I =4.2), which result in radically different structures. In this case the experiment represents the result of four simultaneous dye traces.

hand, islands in experimentally determined Poincaré cuts become visible on the order of 10^1 to 10^2 circulation times and initial placement is less critical. In the experiments the streaklines are stretched into sheets or ribbons and are repeatedly folded in the chaotic regions, revealing typical striated patterns in the Poincaré section. A streakline on a torus is stretched into a ribbon along the surface of the torus; thus, the entire island is revealed in only a few circulations. This flow is successful because the azimuthal circulation time (driven by impeller) and the rate of rotation of the tori are of comparable orders of magnitude (ratio of about 3.5 in our experiments). The robustness of these analog (experimental) simulations lies in their ability to produce connected structures, as opposed to the "peppered-like" appearance of computational results involving the tracking of single particles. Errors in the visualization result from the disturbance in the flow produced by the presence of injection needles, from vibrations, and from geometrical imperfections in the apparatus. Yet, even with these experimental factors, tori generated with the needles in place remain nearly unchanged with time even after 12 hours of operation.

Theoretical analysis with existing tools seems possible only in limiting cases. The unperturbed flow is integrable because of rotational symmetry. For small α and moderate *Re* the experimental results can be treated in terms of perturbation theory of action-angle-angle volume-preserving flows developed by Mézic and Wiggins (*31*). Topological ideas based on flow skeleton arguments, which encapsulate the underlying mathematical structure in terms of fixed points and manifolds, may prove useful as well (*16*).

References and Notes

1. G. B. Tatterson, R. S. Brodkey, R. V. Calabrese, *Chem. Eng. Prog.* **87(6)**, 45 (1991).
2. L. H. Kellogg, *Adv. Geophys.* **34**, 1 (1993).
3. M. Manga, *Geophys. Res. Lett.* **23**, 403 (1996).
4. H. J. Yang and Z. Y. Liu, *ibid.* **21**, 545 (1994).
5. M. G. Brown and K. B. Smith, *Phys. Fluids A* **3**, 1186 (1991).
6. R. B. Pierce and T. D. A. Fairle, *J. Geophys. Res. Atmos.* **98**(D10), 18589 (1993).
7. R. T. Pierrehumbert and H. Yang, *J. Atmos. Sci.* **50**, 2462 (1993).
8. J. M. Ottino *et al.*, *Science* **257**, 754 (1992).
9. J. M. Ottino, *Annu. Rev. Fluid Mech.* **22**, 207 (1990).
10. ———, C. W. Leong, H. Rising, P. D. Swanson, *Nature* **333**, 419 (1988).
11. H. A. Kusch and J. M. Ottino, *J. Fluid Mech.* **236**, 319 (1992).
12. D. J. Lamberto, F. J. Muzzio, P. D. Swanson, *Chem. Eng. Sci.* **51**, 733 (1996).
13. H. Aref, *J. Fluid Mech.* **143**, 1 (1984).
14. S. Wiggins, in *Chaotic Transport in Dynamical Systems* (Springer-Verlag, New York, 1992).
15. M. Hénon, *C. R. Acad. Sci. Paris A* **262**, 312 (1966).
16. R. S. MacKay, *J. Nonlinear Sci.* **4**, 329 (1994).
17. P. Ashwin and G. P. King, *J. Fluid Mech.* **338**, 341 (1997).
18. G. Haller and I. Mézic, *Nonlinearity* **11**, 319 (1998).
19. K. Bajer and H. K. Moffat, *J. Fluid Mech.* **212**, 337 (1990).
20. H. A. Stone, A. Nadim, S. H. Strogatz, *ibid.* **232**, 629 (1991).
21. This flow can be achieved, for example, near the stagnation point of impinging circular jets.
22. J. M. Ottino, *The Kinematics of Mixing: Stretching, Chaos, and Transport* (Cambridge Univ. Press, New York, 1989), pp. 146–148.
23. S. Nagata, *Mixing: Principles and Applications* (Wiley, New York, 1975); G. B. Tatterson, *Fluid Mixing and Gas Dispersion in Agitated Tanks* (McGraw-Hill, New York, 1991).
24. R. C. DiPrima and H. L. Swinney, *Topics in Applied Physics*, H. L. Swinney and J. P. Gollub, Eds. (Springer-Verlag, New York, 1985), vol. 45, pp. 139–180.
25. G. K. Batchelor, *An Introduction to Fluid Dynamics* (Cambridge Univ. Press, New York, 1967), pp. 290–294.
26. P. D. Swanson and J. M. Ottino, *J. Fluid Mech.* **213**, 227 (1990).
27. The supporting sleeve is connected by a series of gears to a motor, allowing rotation in either direction. The impeller is constructed of a 10.16-cm-diameter 0.46-cm-thick acrylic disk mounted on a 1/2-inch (1.27-cm) aluminum shaft that is mounted with a 2.5-cm-tall needle bearing to prevent radial movement. Both motors are controlled manually with Bodine speed controls. An outer rectangular containment vessel is used to minimize optical effects due to curvature.
28. A Liconix 4240NB helium-cadmium constant-wave laser is used with 442-nm blue optics installed. The power rating at this wavelength is a nominal 40 mW and is verified at 36 mW with an Ophir Optronics laser power meter. The sheet is created by using a cylindrical lens mounted on the laser head and aligned such that the sheet falls on the center line of the impeller shaft.
29. C. E. Willert and M. Gharib, *Exp. Fluids* **10**, 181 (1991), see also special issue on Particle Image Velocimetry, J. Kompenhaus and C. Tropea, Eds., *Meas. Sci. Technol.* **8** (December 1997).
30. Each needle has a small radius bend ~3 cm from the end to allow it to project horizontally into the flow. Pressurizing the supply chambers feeding the needles controls the injection rate. To prevent dye "tails" upon repositioning or removal of the needles, the supply pressure is removed and a slight vacuum is applied.
31. I. Mézic and S. Wiggins, *J. Nonlinear Sci.* **4**, 157 (1994).

32. We thank R. Lueptow for assistance with the PIV measurements and I. Mézic for providing comments on a draft of this paper. Supported by the U.S. Department of Energy, Division of Basic Energy Sciences.

25 March 1998; accepted 7 May 1998

Ultraslow Electron Spin Dynamics in GaAs Quantum Wells Probed by Optically Pumped NMR

N. N. Kuzma, P. Khandelwal, S. E. Barrett,* L. N. Pfeiffer, K. W. West

Optically pumped nuclear magnetic resonance (OPNMR) measurements were performed in two different electron-doped multiple quantum well samples near the fractional quantum Hall effect ground state $\nu = \frac{1}{3}$. Below 0.5 kelvin, the spectra provide evidence that spin-reversed charged excitations of the $\nu = \frac{1}{3}$ ground state are localized over the NMR time scale of about 40 microseconds. Furthermore, by varying NMR pulse parameters, the electron spin temperature (as measured by the Knight shift) could be driven above the lattice temperature, which shows that the value of the electron spin–lattice relaxation time τ_{1s} is between 100 microseconds and 500 milliseconds at $\nu = \frac{1}{3}$.

A two-dimensional electron system (2DES), cooled to extremely low temperatures in a strong magnetic field, exhibits many exotic phenomena, such as the fractional quantum Hall effect (FQHE) (*1*). Transport and optical studies of the 2DES have shown that the low-energy physics in these extreme conditions is driven by the electron-electron Coulomb interaction (*2*), but the challenge of precisely describing the low-lying many-body states that exist in a real 2DES remains formidable for both theory and experiment (*3–5*). Such 2DESs have been probed by OPNMR (*6–8*) in the FQHE regime (*9*), which allows the direct radio-frequency (rf) detection of NMR signals from nuclei in electron-doped GaAs quantum wells. The ^{71}Ga OPNMR spectra reveal the local, time-averaged value of the electron spin magnetization, $\langle S_z(\mathbf{R})\rangle$, thus leading to insights about the many-electron states relevant for the FQHE.

We report evidence of ultraslow electron spin dynamics near the most studied FQHE ground state, $\nu = \frac{1}{3}$, with characteristic time scales exceeding ~40 μs below 0.5 K. Although the samples are characterized by "simple" NMR parameters (that is, isotropic

---

N. N. Kuzma, P. Khandelwal, S. E. Barrett, Department of Physics, Yale University, New Haven, CT 06511, USA. L. N. Pfeiffer and K. W. West, Lucent Technologies, Bell Laboratories, Murray Hill, NJ 07974, USA.

*To whom correspondence should be addressed.